

# Modified Densely Connected U-Net with Improved Convolution Deep Belief Network for Lung Cancer Detection on Chest X-Rays

Geetha N.<sup>1</sup>, S. J. Sathish Aaron Joseph<sup>2</sup>

Submitted:25/04/2023

Revised:26/06/2023

Accepted:05/07/2023

**Abstract:** Chest diseases are major health issues that affect people's lives. Early detections of chest disorders are to human lives and numerous approaches have been developed to help with this. Early identification of lung cancer has become critical, and image processing and DLTs (Deep Learning Techniques) have made it possible. Existing EASFMC-based segmentation findings are good for photos with minimal color change and no external disturbance. When artefacts are present, however, the algorithm performs badly. The algorithm, for example, mistakenly recognizes the black border, medical gauze, and other dark things as lung cancer. Lung patient scan images were used in this investigation to detect and classify lung nodules, as well as to determine their malignancy level. The NIH Chest-Xray pictures are segmented using the Modified DenseU-Net architecture and the Adaptive Butterfly Optimization Algorithm for hyper parameter tuning (ABOA) The segmentation pipeline given here comprises of two DLTs: Enhanced U-Net, which was originally created for biomedical image segmentation, and Improved convolutional deep belief network (ICDBN) for lung nodule detection with their level. The U-Net model performs semantic segmentation on the images before sending them to the ICDBN for final normal/abnormal classification. The lung nodules are classified and the amount of malignancy is determined with excellent accuracy utilizing this design.

**Keywords:** Chest diseases, lung cancer, NIH Chest-Xray, Modified DenseU-Net architecture, Adaptive Butterfly Optimization Algorithm, and Improved convolutional deep belief network are some of the terms used in this paper.

## 1. Introduction

Medical X-rays are pictures utilized to diagnose delicate areas of the human body like teeth, chest, bone and head. Medical professionals have utilized this technology for decades to analyze abnormalities in human organs and fractures of the bone [1]. This mainly due to the fact that they are noninvasive, inexpensive and excellent diagnostic instruments for detecting pathological abnormalities [2]. Xrays of the chest or CXRs (Chest X-Rays) can be used to identify cavities, infiltrates, blunted costophrenic angles, and even tiny widely scattered nodules. Radiologists use Xrays to identify pleurisies, effusions, pneumonia, bronchitis, infiltrations, nodules, atelectases, pericardites, cardiomegalies, pneumothorax, fractures, and other conditions or disorders and diseases [3]. Radiologists regard classifying abnormalities based on CXRs to be a time-consuming task; hence various algorithms have been proposed to help them do it accurately [4]. Though over the years, CADs (Computer-aided diagnostics) have been proposed for extracting helpful information from X-rays

and help clinicians in acquiring quantitative knowledge, they have not have gained a significant amount of relevance in X-ray diagnosis [5]. As a result, their role has been confined to providing visualization functionality to assist clinicians in their decision-making.

The preceding study works were effective in diagnosing medical conditions; however, when compared with DLTs, their performances have been wanting in terms of accuracies, computational times, and errors. DLTs have been used to improve picture categorization accuracies [10, 11]. In performing such tasks, these DLTs have demonstrated much better accuracies, inspiring studies to explore medical images with similar networks for illness classifications where DLTs could extract important characteristics and separate classes of images. The issue of categorizing CXRs with lung disorders has become more practical due to MLTs (machine learning techniques). DLTs have been utilised in particular to complete this goal [6]. DLTs are a sort of machine learning that develops patterns that may be employed in decision-making and is inspired by the human brain's architecture [7]. The most extensively used DLT architecture is CNNs (Convolution Neural Networks). CNNs have been used to classify a range of medical images [8] because to its ability to extract varying levels of information from images.

<sup>1</sup>(Reg No. BDU2120412778980) Research Scholar in Computer Science, J.J college of Arts and Science (Autonomous), Sivapuram Post, Pudukkottai (Affiliated to Bharathidasan University, Tiruchirapalli), Tamil Nadu, India. Email-geethavelu08@gmail.com

<sup>2</sup>Assistant Professor and Research Advisor in Computer Science, (Ref.No:05526/Ph.D.K 10/Dir/Computer Science/R.A), P.G and Department of Computer Science, J.J.College of Arts and Science (Autonomous), Sivapuram, Pudukkottai, Tamil Nadu, India. Email-satjoe7@gmail.com

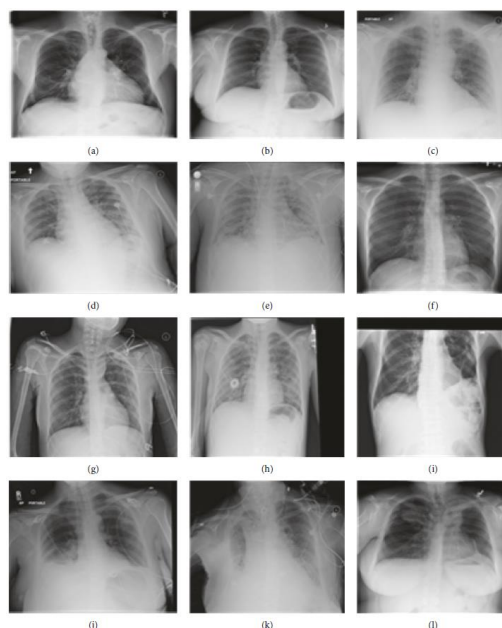


**Fig.1.** CXRs diseases [10]: (a) Atelectasis. (b) Cardiomegaly. (c) Consolidation. (d) Edema. (e) Effusion. (f) Emphysema. (g) Fibrosis. (h) Infiltration. (i) Mass. (j) Nodule. (k) Pneumonia. (l) Pneumothorax.

Following the findings of prior research works, DCNNs (deep CNNs) are employed In this study to increase the accuracy and minimize the MSEs (Mean squared errors) in the diagnosis of chest illnesses [9]. To categorize lung illnesses and provide comparison data, traditional and DLT-based networks are employed. CNNs may be used to characterize 12 frequent illnesses found on CXRs s, as shown in Fig. 1 [10]: atelectasis, cardiomegaly, effusion, infiltration, mass, nodule, pneumonia, pneumothorax, consolidation, edoema, emphysema, and fibrosis. Using NIH CXRs dataset, this work attempts to train both conventional and DLTs while evaluating their performances using segmentation. The following are the work's key contributions:

- This work's used NIH CXRs image dataset may be found in the Kaggle repository [11], and is an open source.
- When the filter's scale matches the size of the local structures, Hessian-based multiscale filtering reacts best, suggesting that scale selection is based on the best response among multiple scales. As a consequence, the greatest reaction in the immediate vicinity may be utilized to extract local structures..
- Segmentations are executed using modified DenseU-Nets where U-Net structures use modified residual layers for block unit convolutions, together the benefits of the inception method with the ability to input multi-scale picture data.
- Finally, the ICDBN method was effectively deployed on the previously described dataset to classify lung disease by predicting lung disease from X-ray pictures and using the Adaptive Butterfly Optimization Algorithm for CDBN hyper parameter optimization.

The following is the format of this paper: The approaches for diagnosing chest problems using DLTs are presented in Section 2. In Section 3, in addition to the database description, the suggested DL model for diagnosing chest disorders is described, as well as its operational principles. Section 4 compares the performance of the networks utilized in simulations and discussions, and Section 5 concludes the paper with recommendations for future improvements.

## 2. Related Work

In the realm of lung cancer detection, more DL algorithms have been applied in recent years. In this study, Wang et al. [12] proposed weakly supervised approach for classifying whole-slide lung cancer images quickly and accurately. Their technique retrieved discriminative blocks using patch-based FCNs (fully convolutional networks) and subsequently produced representative deep features with 97.3 percent accuracy. Yu et al. [13] combined AHMMs (Adaptive Hierarchical Heuristic Mathematical Models) with DLTs to investigate previous therapy schemes in the creation of automated radiation adaptation methods for NSCLCs (Non-Small Cell Lung Cancers) with low rates of grade 2 RP2 radiation pneumonitis and with the goal of optimizing local tumour controls. Image captures, pre-processes, binarizations, thresholds, and segmentations, as well as feature extractions were all a part of the proposed system. Their DNN identification scored 96.67 % in terms of accuracy.

Chen et al. [14] suggested LDNNET, which employed Dropouts, Dense-Blocks, and Batch Normalizations to address these difficulties. The LDNNET was convnet-based adaptive architecture that used softmax classifiers to overcome challenges of deep convnets. Their results obtained were LUNA16, specificity (0.994585), accuracy

(0.988396) and sensitivity (0.982072), but on Kaggle's DSB 2017, their corresponding values were 0.999480, 0.999652, and 0.998974. Furthermore, the AUC for both datasets exceeds 0.98. Liu et al. [15] developed an automated lung nodule analysis system. In [17] suggested a two-path CNNs that "denoized first" to address this difficulty (DFD-Net). The given model included comprehensive denoising and detection components. To reduce noises, residual learning denoising models (DR-Nets) were used during the preprocessing stage. The demonized pictures from DR-Nets were then fed into two-path CNNs, which diagnosed lung cancers. Suresh and Mohan [18] extracted self-learned features and compared their results with other traditional diagnostic systems using an end-to-end learning CNN. Using GAN produced pictures, our suggested CNN obtained 93.9 percent classification accuracy, 93 percent average specificity, and 93.4 percent average sensitivity, with the maximum

observed value of 0.934 for ROC (receiver operating characteristic) curve values.

Yamunadevi and Ranjani [19] proposed efficient and adaptive segmentations based on fuzzy GLCM that enabled detections of lung cancers early and in simple ways which benefitted both clinicians physicians and patients in terms of accurate initiations of treatments. Cancerous growths were categorized using GoogLeNet's CNN architecture to identify benign/malignant types of cancers. Sori et al. [20] suggested deeper architectures of CNN for the same issue. The study generated suspicious nodules using modified version of U-Net as inputs. Their multi-path CNN could identify lung cancers using both local and global contextual information. With the widespread usage of digital cameras, hand wound imaging has become a standard practise in research settings.[28],[29]. Table 1 lists the benefits and drawbacks of DL approaches, along with dataset specifics.

**Table 1.** The advantages and disadvantages of DL methods with dataset details

Author	Method	Database images	Advantages	Disadvantages
Wang et al. [12]	fully convolutional network	lung cancer WSI dataset	It uses image-level labels, as well as some coarse annotations, to do weakly supervised learning.	For the following therapeutic treatment of patients, an accurate and exact diagnosis is crucial.
Yu et al., [13]	deep neural network	CT pictures from <a href="http://diagnijmegen.nl/">http://diagnijmegen.nl/</a>	The threshold process removes unnecessary peaks in pixels in a lung cancer medical picture.	The main stumbling block is a diversity of diverse tumour patterns found in high magnification fields.
Chen et al. [14]	LDNNET	LUNA16 and Kaggle DSB 2017	Dense Blocks which enhance accuracy, assisted LDNNET networks to learn is better for classifications of lung nodules.	Developing a large-scale training dataset is tough because pixelwise demarcated annotations on pictures are time overwhelming and tiresome.
Liu et al., [15]	MTMR-Net	LIDC-IDRI dataset	The diagnostic findings with internal relationships clearly investigated in our model have seen some comparable patterns in practical use	The number of lung CT scans in current datasets were small with significant nodule/non-nodule ratios in samples, reducing performances of neural networks in training.
Liu et al., [16]	deep neural network	TCGA dataset and ICGC dataset	It has a quick learning curve and good accuracy	The curse of dimensionality and unbalanced data, on the other hand, are the most significant problems in mining gene expression databases.
Sori et al. [17]	DFD-Net	CT scan image	This sort of model can readily minimise picture noise	The server performance requirements, on the other hand, are greater.
Suresh & Mohan [18]	CNN	Lung CT Image Database consortium public repository	The trained network's architecture is pre-trained and fine-tuned	The architecture of trained networks were pre-trained and fine-tuned, resulting probable aggregates of nodule detections and minimizing false positives..
Yamunadevi & Ranjani [19]	GoogLeNet CNN	images obtained using bronchoscopy	The diagnostic findings with internal relationships clearly investigated in our model have seen some comparable patterns in practical use	However, determining if these are actual nodules will take a significant amount of time and work.
Sori et al. [20]	deep CNN	Kaggle Data Science Bowl 2017	Following convergence, it was discovered that the CNN had a higher generalisation power for determining cancer.	The number of segments must be chosen ahead of time owing to the high time and space complexity.

Inference: The literature and dataset related to DLTs in lung cancer analysis have been thoroughly reviewed in this study. Although the work reviewed for this review uses a variety of off-the-shelf architectures, there is little evidence to suggest that one based on deep CNN beats another for lung cancer detection. Many articles compare multiple architectures for the same task, although the differences

between the results are usually minor. This is commonly done with CT scan images, but X-ray images are rarely explored. Previous studies similarly overlooked label errors and overlap, as well as the therapeutic use of such generic image-level methods. A large proportion of articles were rejected due to insufficient scientific quality. This research proposes a unique DLTs strategy based on

enhanced convolution deep belief networks to handle these challenges.

### 3. Proposed Methodology

As indicated in Figure 2, ICDBNs are presented in the work for the diagnosis of chest disorders, and they are trained and evaluated on the same CXRs database. When filter scales match local structure sizes, responses of

Hessian-based multi-scale filters are better implying that scale selections are based on strongest interactions between scales. The researchers then presented a modified denseU-Net semantic segmentation network to improve the segmentation outcomes of deep and superficial regions in chest pictures. The NIH Chest-Xray-14 database has been effectively used to categorize lung illness using a new ICDBN.

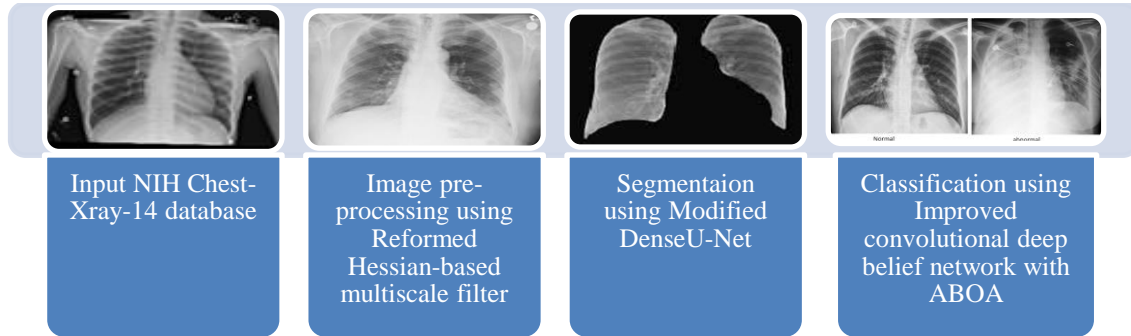


Fig.2. General Framework Diagram

#### 3.1. Input Image Database and Filtering method

The suggested model is tested using a dataset of NIH CXRs images from the Kaggle library. Both the complete and model versions of the dataset are considered. Hessian-based multi-scale filters enhanced performances by combining Hessian matrices with Gaussian convolutions to tailor filtering responses of many scales. Vascular architecture for better medical outcomes. The study of eigenvalues from scaled Hessian matrices using filters. The Hessian matrix's eigen vectors and eigenvalues are strongly connected to vascular intensity and direction. The Hessian matrix  $I(x,y)$  for a single input image is a 2x2 matrix made up of input image's second-order partial derivatives, as shown in (1):

$$HM(x, y) = \begin{pmatrix} \frac{\partial^2 I}{\partial x^2} & \frac{\partial^2 I}{\partial x \partial y} \\ \frac{\partial^2 I}{\partial x \partial y} & \frac{\partial^2 I}{\partial y^2} \end{pmatrix} \quad (1)$$

Like images  $I$ , Hessians are also discrete functions that can be approximated as continuous functions utilizing 2-dimensional GF (Gaussian filter) (2) and convolutions differentiations in properties according to (3)

$$GF(x, y, \sigma) = \frac{1}{\sqrt{(2\pi\sigma^2)^3}} \exp\left(-\frac{1}{2} \left(\frac{x^2}{\sigma_1^2} + \frac{y^2}{\sigma_2^2}\right)\right) \quad (2)$$

$$HM(x, y) \approx GF(x, y, \sigma) * \begin{pmatrix} \frac{\partial^2 I}{\partial x^2} & \frac{\partial^2 I}{\partial x \partial y} \\ \frac{\partial^2 I}{\partial x \partial y} & \frac{\partial^2 I}{\partial y^2} \end{pmatrix} \quad (3)$$

$$= \begin{pmatrix} \frac{\partial^2 GF}{\partial x^2} & \frac{\partial^2 GF}{\partial x \partial y} \\ \frac{\partial^2 GF}{\partial x \partial y} & \frac{\partial^2 GF}{\partial y^2} \end{pmatrix} * I(x, y)$$

where  $GF(x,y)$  implies scaled kernels from Gaussian convolutions. Let  $| \cdot |$  be the convolution symbol,  $\epsilon_1$  and  $\epsilon_2$  be the eigenvalues of  $HM(x,y)$ ,  $EV_1$  and  $EV_2$  be the associated Eigen vectors, and  $*$  be the eigenvalues of  $HM(x,y)$ , and  $EV_1$  and  $EV_2$  be the associated Eigen vectors. Because  $|\epsilon_1|$  has smaller magnitudes corresponds to eigenvector  $EV_1$ , which point in least curvature directions, whereas  $|\epsilon_2|$  corresponds to eigenvector  $EV_2$ , which point in the direction of largest curvatures. These demonstrate  $u_1$  parallelism to longitudinal axes of blood arteries and  $|\epsilon_1| \approx 0$ , while  $EV_2$  was parallel to radial axes. Two metrics were developed based on these data to assess anisotropy and contrasts of pixels. The figures were obtained using (4) and (5) and depicted in Figure (5). Ratio anisotropy, the first ratio, compensates for variations in blob-like forms, but cannot point out differences between line and plate like patterns. To discriminate between plate-like and line-like structures, the second ratio contrast is used.

$$ratio_{anisotropy} = \frac{|\epsilon_1|}{|\epsilon_2|} \quad (4)$$

$$ratio_{contrast} = \sqrt{|\epsilon_1|^2 + |\epsilon_2|^2} \quad (5)$$

Throughout the categorization phase, the smaller the ratio anisotropy, the more likely the pixel is to be part of a

tumour. When eigenvalues from small contrast are marginal, contrast ratios were lower, and the higher the ratio contrast, the more probable the pixel is a malignancy. The curvatures will have negative values for images when vessels are darker than backgrounds implying valleys are cancers, hence these findings prompted generation of likelihood functions commonly called "malignant equations"(6), for scales  $sc$ .

$$C_0(sc) = \begin{cases} 0 & \text{if } |\epsilon_2| > 0 \\ e^{-\frac{ratio_{anisotropy}^2}{2th1^2}} \left(1 - e^{-\frac{ratio_{contrast}^2}{2th2^2}}\right) & \text{otherwise} \end{cases} \quad (6)$$

where  $th1$  and  $th2$  are thresholds that control sensitivity of line filters for measures of  $R_a$  and  $R_b$ . Table 1 shows the patterns that can be assumed by combining the ordered eigenvalues ( $|\epsilon_1|, |\epsilon_2|$ ) for two dimensional chest images. Table 2: Possible Two dimensional patterns based on eigenvalues with +/- signs.

$\epsilon_1$	$\epsilon_2$	Orientation Pattern
Noisy	Noisy	Noisy with no preferred direction
Low	High-	Bright with tabular structure
Low	High+	Dark with tabular structure
High-	High-	bright(Tiny blob-on-a-stick like structures)
High+	High+	dark(Tiny blob-on-a-stick like structures)

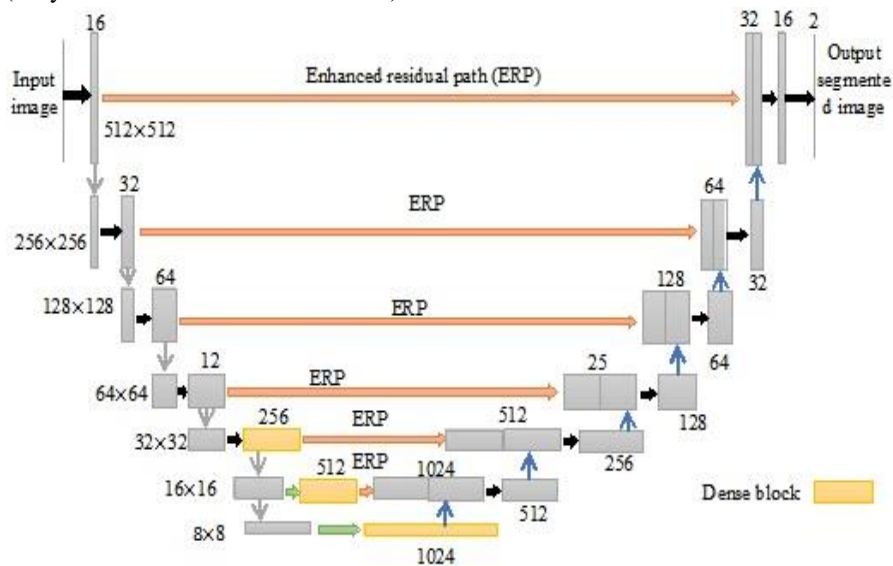


Fig.3. Architecture of Modified Dense-UNet

Dense-kUNet is a cross of ER-UNet and Dense-UNet. With  $k=1$ , Figure 3 shows a sample of its layout. It combines the extraction of dense features with the progressive extraction of features to a finer scale using the ER-approach UNet. DenseUNet's submodule's upsampling component is skip-connected to the succeeding Dense-max UNet's pooling sections, similar to U-Net are comparable to transferring coarser inputs to subsequent sub-modules to create better image segmentations. An abbreviation for "improved residual path" is ERP (enhanced residual path). UNet provides a shortcut link between the convolution and

### 3.2. Image segmentation using Modified dense-UNet

This study presents a modified dense-UNet for segmenting CXRs images where modifications involved embeds of dense blocks into U-Net, resulting in deeper layers for increased feature extraction based on both U-long Net's long and short skip connection features. Secondly, Dense-UNet [21] and U-Net were combined with improved residual block (ER-UNet) to create modified dense-UNet, a network composed of many Dense-UNet submodules. Skip links are established among nearby submodules to aid the model's discovery of fine characteristics by efficiently transmitting data.

In [22], the authors employed dense connections for better outcomes. In their schema, layers received preceding layer's inputs and passed on their own feature-maps to succeeding layers. As a result of these dense block designs, networks become thinner and more compact, improving computational and memory efficiencies. In reality, all convolution layers use 33% kernels with a stride size of 1. 3 x 3 kernels with stride sizes of 2 were applied on sampling layers. ReLUs served as activation functions and normalizations of batches reduced over fits while enhancing learning rates of the model.

de-convolution layers to reduce information loss during the pooling phase. While the convolution layer's characteristics are calculated at the network's early stages, they are low-level features; the de-convolution layer's characteristics are computed at the network's deeper levels, making them higher-level features. The low-level features must be handled before the features can be merged since the convolution and de-convolution layers convey different types of features.

The combination of these two mismatched feature sets may obstruct the prediction process, resulting in some

discrepancies in the overall learning process. Instead of integrating convolution and de-convolution layer features directly, suggest merging numerous convolution layers via the shortcut connection to alleviate the feature disparity between the convolution layer and the de-convolution layer. Convolution of low-level features improves learning, then three convolution processes are used to extract deeper features and residual structures. Before merging the input and output dimensions, use a 1 1 convolution block to mix them. An experimental comparison is used to establish the number of convolutions to use. Increasing convolutions counts do not impact results, but add large number of parameters, therefore in the E-Res route Layer, I picked 6 convolutions.

The 2 2 max pooling procedure is shown by the grey arrow, whereas the upsampling operation is represented by the blue arrow. The red arrow indicates omitted lengthy links between max pooling layer and specified upsampling layer ERP. After the network's max pooling, three dense blocks are integrated instead of the initial two-convolution blocks using batch normalization and the ReLU activation function. The figure depicts these dense chunks as yellow rectangular blocks with green arrows indicating critical operations. Using the dense process, set the input  $x$  to get the result  $y$ . Like DenseNet, preceding layer's feature maps,  $x_0, \dots, x_m$ , are supplied into the  $m$ th layer ( $m-1$ )

$$x_m = F_m([x_0, x_1, \dots, x_{m-1}]) \quad (7)$$

Where  $[x_0, x_1, \dots, x_{m-1}]$  stands for concatenated feature maps generated in layers  $0, \dots, m-1$ , and  $F_m$  are functions from 3 consecutive operations namely batch normalizations (BN), ReLU, and 3 x 3 convolutions. Dense blocks generate  $F_m$  feature maps, where  $m$  implies network growth rates. Given  $m_0$  channels counts of input layers, input feature map counts in  $m$ th layers are:  $m_0 + k(m-1)$ . It's worth noting that a 1 x 1 convolution is used to minimise the complexity and size of dense blocks, followed by a 3x3 convolution input, which can significantly reduce the amount of work while maintaining the model's accuracy. ResNet's bottleneck layer is likewise constructed in this manner.

The modified dense-UNet model's internal operation is similar to Dense-UNet, with the grey arrow indicating The black arrow indicates max pooling of 22 scale, and the blue arrow indicates upsampling operation, the operation green arrow indicates is compatible with Dense-UNet, and the red arrow indicates skip connections between neighbouring submodules. The dense block is represented by the yellow rectangular block, which has the same concept and implementation as the Dense-UNet. Six downsampling phases are followed by six upsampling stages in the submodules. The long skip connection within the submodules equates to six skip connections between nearby submodules. The ER-UNet structure can help finer feature extraction by transferring coarser scales to

succeeding modules. Dense-UNet makes use of DenseNet's feature extraction capabilities, whereas ER-UNet exponentially expands the network's input window size. CDBN and ACO have improved lung cancer detection.

### 3.3. Lung Cancer detection using Improved CDBN with ACO

A multilayer of restricted Boltzmann machines (RBM) is layered on top of each other in the DBN [22] to extract deep features from a picture. Equation (8) depicts joined potential allocations between inputs  $v$  and  $l$  hidden layers in visible layers. The data weights are calculated using unsupervised greedy techniques. The first layers of RBMs are trained for establishing the layer's trainable parameters and the outputs from hidden layers are then used as inputs for second layer's RBM. Thus, the first layer's parameters are learned gradually. Softmax regression classifiers coupled with ultimate hidden layers, and SGDs (supervised gradient descents) are employed in fine tuning (Almanaseer et al., 2021; Dai et al., 2020).

$$\Pr(x_m, hl^k) = \left( \sum_{k=0}^{l-2} \Pr(hl^k | hl^{k+1}) \right) \Pr(hl^{l-1}, hl^l) \quad (8)$$

$$w = w + \varepsilon(hl_1 x'_1 - V(hl_2 = 1 | x_2) x'_2) \quad (9)$$

$$bias = bias + \varepsilon(x_1 - x_2) \quad (10)$$

$$v_{bias} = v_{bias} + \varepsilon(hl_2 = 1 | x_2) \quad (11)$$

$\Pr(hl^{l-1}, hl^l)$  is the probability distribution among the visible and hidden layers of the topmost RBM. Following setup, a set of  $x_m$  training feature maps is provided. The visible layers ( $v$ ) in the RBM network structure are  $k$ , with the  $j$ th hidden levels affecting the visible layers only after launch. The training duration and learning rate are presented once each parameter has been specified. The similar distribution strategy is used to alter the training parameters. If the method is successful, the output will continue; otherwise, the parameter training will proceed on the basis of (9 to 11). After starting, the first layer of RBM is trained. The hidden layer is then used to train the first RBM layer as well as as input to the second, and so on until the final RBM layer is learned. Finally, the output of this layer is used as a classifier by the fine-tuned softmax regression.

Where bias is the bias of each hidden group,  $V$  is a vector consisting of  $V(hl_2=1 | x_2)$ ,  $w$  is the weight element in the row and column of the filter, and all visible units have the same bias  $v_{bias}$ . CDBNs frequently employ convolutional Restricted Boltzmann machines (CRBMs). CNNs use filters to establish connections between the layers rather than to investigate an item Unlike the DBN design, where each visible layer neuron is coupled to each hidden layer neuron, the CNN's neurons are not totally connected to one another. There are no connections between nodes of visible layers. Hidden nodes do not get connected that have

undirected connections with other in graphical topologies of basic RBMs. Feature extractors like CDBN are being used more for recognizing patterns to build hierarchical structures of features. CDBN models can also draw accurate probabilistic conclusions in both bottom up and top down approaches. Many layers of max-pooling CRBMs are layered on top of these structures, and training processes are carried out using greedy techniques in layers similar to conventional DBNs. The systems learn higher level features like stroke groups and object components by constructing CDBNs.

Two layers of CRBM were trained in system tests and feed forward approximations used for inferences. CDBNs are constructed on top of CRBMs where series of CRBMs teach CDBNs with one CRBM flowing into the next. The visible and hidden layers are connected via the local and shared parameters of CRBM architectures. Real-valued units can be displayed, but binary-valued units cannot be seen [23]. Three convolutional layers and three separate max-pooling layers are used in this research. The kernel window is set to a size of 22 pixels, and increased filter counts in layers to accommodate complex visual patterns in training. This work used 128x128 images with a batch size of 200 for testing.

The CDBN method described above is fed pre-processed attribute vectors through the first layer's output. The inputs are processed sequentially, with each iteration involving a matrix multiplication with the weighted matrix  $w$ , as well as the addition of bias bias. The ICDBN's ultimate output is a likelihood of lung cancer locations that are labeled for predicting. Initial weights, activation functions, learning rates, iterations and epochs, are just a few of the hyper-parameters that were investigated. The hyper-parameters include counts of convolution layers, kernels, and their sizes.

**CDBN ACO-based hyper-parameters:** The numerous of nodes in the hidden layer, as well as the number of bias and weight as hidden layer nodes in CDBN, have a direct impact on learning results due to their non-linear mapping ability and learning accuracies while updating data. This algorithm is a great optimization algorithm because it is based on Ant's behaviour. Ants are continually on the lookout for food in an ad hoc fashion. They use pheromone to clearly identify their search pathways when they find food [24]. The quality and quantity of food found influence the amount of pheromone generated. A greater number of high-quality food channels is indicated by a higher pheromone concentration. Other ants use pheromone concentrations to find food and bring it back to their colonies. As a result, ideal hyperparameters are defined by pheromone concentrations.

Additionally, the population density affects how many people are needed to convey food. When ants search globally, they are in their final state and leave behind pheromones that other ants follow. As a result, after they

have reached their ultimate condition, their actions attempt to spread pheromones. As previously mentioned, the accuracy of the proposed CDBN model is based on hyper-parameters. The ACO algorithm is also referred to as the ACO-CDBN model since it optimises hyper-parameters. The suggested model is a crop yield recommender system since it is used to calculate crop yields. ACO's global modifies CDBN's hyper-parameters to optimise and boost performance. The objective function in this study was f-measure, which was used to assess the fitness of ant sites. The searches and optimizations of this work are proposed for lung cancer detections with accurate predictions and depicted in Figure 4.

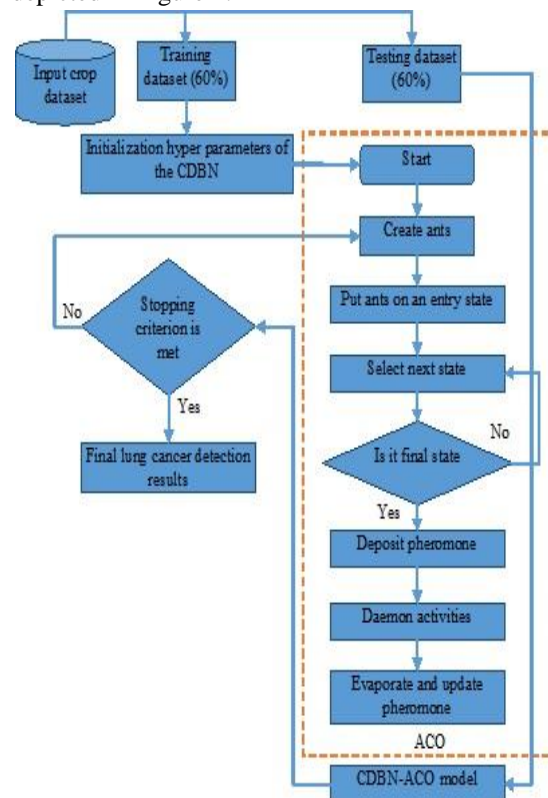


**Fig. 4.** Flowchart of the ant colony and optimization of CDBN-ACO

#### 4. Experimental Results and Analysis

The suggested project CDBN-ACO divides the gathered data into two categories: normal and malignant. Because the noise in lung X-ray pictures is often high, the first stage in the task is to use using pre-processing methods to eliminate unwanted and noisy data before starting the analysis. The cancer area will then be recovered after these photos have undergone a segmentation process. The segmented images are input into the suggested DSCNN-MBOA for lung cancer detections, with MBOA based feature selections. The performances of this work's suggested schema is compared with existing methods including transfer learning [25], modified AlexNet [26], VDSNet [27], CNN with and DSCNN-MBOA using a variety of parameters, including accuracy, precision, F1-score, execution time, specificity, and sensitivity.

$$\text{Accuracy} = (\text{TP} + \text{TN}) / (\text{TP} + \text{TN} + \text{FP} + \text{FN}) * 100 \quad (12)$$

$$\text{Precision} = \text{TP} / (\text{TP} + \text{FP}) * 100 \quad (13)$$

$$(2 * \text{Precision} * \text{Recall}) / (\text{Precision} + \text{Recall}) \text{ F1 score} \quad (14)$$

$$\text{Specificity} = \text{TN} / (\text{TN} + \text{FP}) * 100 \quad (15)$$

$$\text{Sensitivity} = \text{TP} / (\text{TP} + \text{FN}) * 100 \quad (16)$$

Where, TP stands for True Positive and it refer to the total number of positive lung pictures that have been identified as malignant. FN stands for False Negative, and it refers to the total number of lung pictures that are now positive but are categorized as normal since they are negative. True Negative (TN) refers to the total number of lung pictures that are currently negative and have been labelled as such. False Positive (FP) refers to the overall lung pictures that are currently negative but have been categorized as positive.

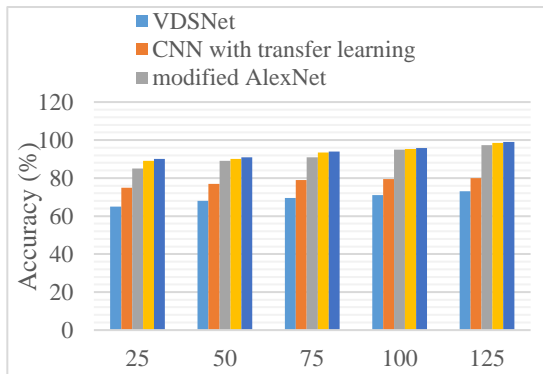


Fig.5. Accuracy performance comparison

Figure 5 displays the accuracy of recommended and existing models for the number of characteristics in a particular database. With a value of 98.95 %, the proposed CDBN-ACO improves accuracy. In comparison to the regular VDSNet, modified AlexNet, CNN with transfer learning, and DSCNN-MBOA, the proposed method is more effective in two ways. One advantage of the suggested deep model is that it incorporates the benefits of both the normal DBN and CNN. The other is that ACO-based hyper parameter adjustment improves the proposed deep model's learning capabilities.

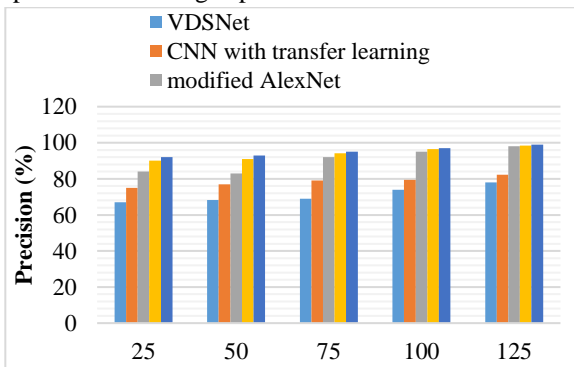


Fig.6. Precision performance comparison

Figure 6 displays the accuracy of current and planned models for the quantity of attributes in a certain database. Precision increases along with the amount of characteristics. When compared to the VDSNet, modified

AlexNet, CNN with transfer learning, and DSCNN-MBOA, the CDBN-ACO achieves an accuracy of 98.96%. The main justification is that the learnt features will almost surely be overcomplete if the hidden units have a larger sparse coefficient (greater activity).

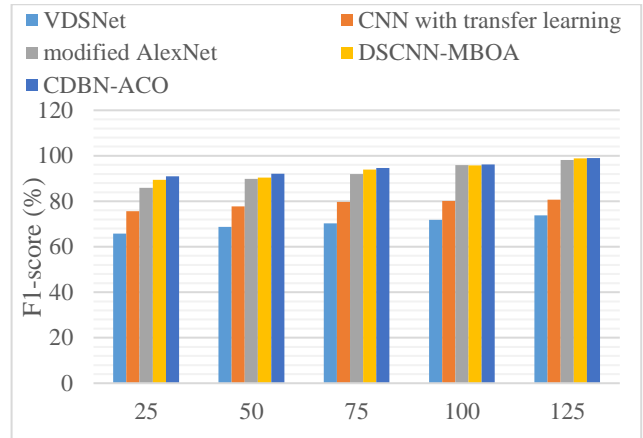


Fig.7. F1-score performance comparison

Figure 8 depicts planned and current models' F1 scores for characteristics in the supplied datasets. The f-measure grows along with the amount of characteristics. When compared to other models like VDSNet, modified AlexNet, and CNN with transfer learning, the CDBN-ACO has an f-measure of 98.96%. This is happening because the ACO is successfully modifying the CDBN parameters with a high F1-sore. rate, which is beneficial in lung cancer diagnosis.

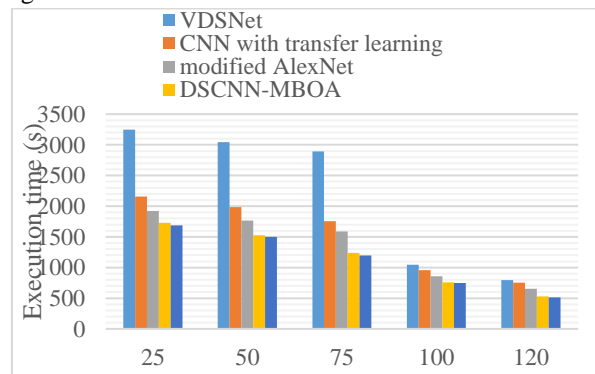


Fig.8. Execution time performance comparison

Figure 8 displays the execution times of proposed and existing models for the number of features in a specific database. The time it takes to execute each feature increases as the number of features does. The CDBN-ACO had a recall of 514.25s when compared to the VDSNet, modified AlexNet, CNN with transfer learning, and DBCN-ACO. The findings show that using CDBN-ACO to address the issue of CXRs diseases is promising in terms of correctly identifying related or complex problems with high identification rates.

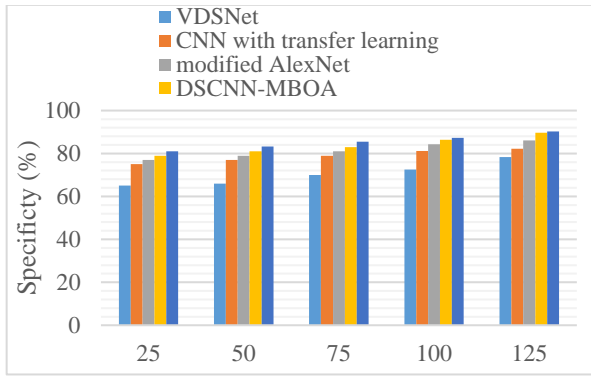


Fig.9. Specificity performance comparison

The specificity of suggested and current models for the amount of features in a given database can be seen in Fig.9. The recall is increased as the number of features is increased. When compared to the VDSNet, modified AlexNet, CNN with transfer learning, and DBCN-MBOA, the CDBN-ACO achieves a recall of 89.65%. Existing techniques are underfitting because they are simplistic models that are inadequate for high-dimensional datasets. It can be seen that the suggested modified Dense U-Net algorithm not only has a high level of segmentation accuracy, but also has a high level of stability and universality.

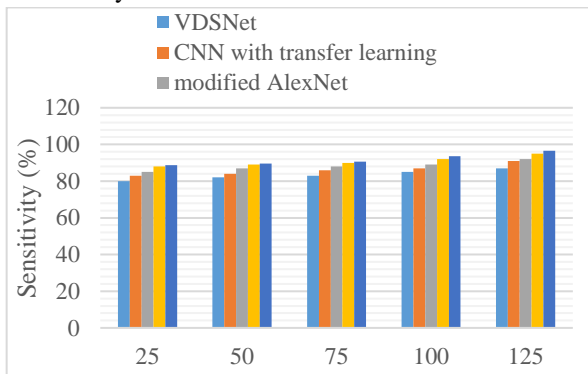


Fig.10. Sensitivity performance comparison

Figure 10 illustrates how sensitive proposed and current models are to the number of characteristics in a particular database. CDBN-ACO significantly enhances accuracy and sensitivity values when compared to VDSNet, modified AlexNet, CNN with transfer learning, and DBCN-MBOA by a factor of 96.56%. The proposed method therefore beats existing algorithms in terms of promising validation results for cancer predictions. Furthermore, it should be noted that the CNN takes slightly longer to converge than other methods. As a result, this is due to the depth of CDBN's structure, which takes a long time to compute, especially when there are a lot of inputs. In comparison to other networks, however, this ideal deep structure is the most critical aspect in getting a better recognition rate.

## 5. Conclusion and future work

In order to diagnose chest conditions, CDBN-ACO was trained on and put to the test on CXR pictures showing a

variety of illnesses. A huge number of iterations and a variety of learning parameters were used in several trials to train these networks. A modified Dense U-Net technique based on dilated convolution and ERP was used to distinguish between the contour of deep cancer and superficial cancer. Based on the U-Net network, the proposed network for muscle segmentation includes a dilated convolution module and ERP to improve its performance. Even though the needed computing time and iterations were almost same, it was found after convergence that the CDBN-ACO had greater generalization capability than existing methods. The CDBN-deep ACO's structure is largely responsible for this outperformance, which makes use of the power of extracting different level features to improve generalization. The outcome of the simulation for lung cancer detection. In comparison to the suggested network, these networks have poorer generalization and accuracy capabilities. The obtained findings show that the suggested CDBN-ACO has a high recognition rate. The Deep Q Network (DQN), which classifies medical data by deliberately interacting with contextual data and extracting anisotropic properties, would also be examined.

## References

- [1] Malone, J. (2020). X-rays for medical imaging: Radiation protection, governance and ethics over 125 years. *Physica Medica*, 79, 47-64.
- [2] Zimek, Z. (2020). Economical evaluation of radiation processing with high-intensity X-rays. *Nukleonika*, 65.
- [3] Jaiswal, A. K., Tiwari, P., Kumar, S., Gupta, D., Khanna, A., & Rodrigues, J. J. (2019). Identifying pneumonia in chest X-rays: a deep learning approach. *Measurement*, 145, 511-518.
- [4] Ge, Z., Mahapatra, D., Sedai, S., Garnavi, R., & Chakravorty, R. (2018). Chest x-rays classification: A multi-label and fine-grained problem. *arXiv preprint arXiv:1807.07247*.
- [5] Rahmat, T., Ismail, A., & Aliman, S. (2018). Chest x-rays image classification in medical image analysis. *Applied Medical Informatics*, 40(3-4), 63-73.
- [6] Ahmed, A., Tharwat, G., Bouallegue, B., Khattab, M., Al Moustafa, A., & Matter, S. (2021). Classification of chest x-ray images using machine learning techniques.
- [7] El Asnaoui, K., Chawki, Y., & Idri, A. (2021). Automated methods for detection and classification pneumonia based on x-ray images using deep learning. In *Artificial intelligence and blockchain for future cybersecurity applications* (pp. 257-284).
- [8] G. Litjens, T. Kooi, E. B. Bejnordi et al., "A survey on deep learning in medical image analysis," *Medical Image Analysis*, vol. 42, pp. 60–88, 2017.
- [9] Labhane, G., Pansare, R., Maheshwari, S., Tiwari, R., & Shukla, A. (2020, February). Detection of pediatric pneumonia from chest X-ray images using CNN and transfer learning. In *2020 3rd International Conference on Emerging Technologies in Computer Engineering: Machine Learning and Internet of Things (ICETCE)* (pp. 85-92). IEEE.

- [10] Abiyev, R. H., &Ma'aitaH, M. K. S. (2018). Deep convolutional neural networks for chest diseases detection. *Journal of healthcare engineering*, 2018.
- [11] NIH sample Chest X-rays dataset, <https://www.kaggle.com/nih-chest-xrays/> sample , Accessed 28th Jun 2020
- [12] Wang, X., Chen, H., Gan, C., Lin, H., Dou, Q., Tsougenis, E.,&Heng, P. A. (2019). Weakly supervised deep learning for whole slide lung cancer image analysis. *IEEE transactions on cybernetics*, 50(9), 3950-3962.
- [13] Yu, H., Zhou, Z., & Wang, Q. (2020). Deep learning assisted predict of lung cancer on computed tomography images using the adaptive hierarchical heuristic mathematical model. *IEEE Access*, 8, 86400-86410.
- [14] Chen, Y., Wang, Y., Hu, F., Feng, L., Zhou, T., &Zheng, C. (2021). LDNNET: Towards Robust Classification of Lung Nodule and Cancer Using Lung Dense Neural Network. *IEEE Access*, 9, 50301-50320.
- [15] Liu, L., Dou, Q., Chen, H., Qin, J., &Heng, P. A. (2019). Multi-task deep model with margin ranking loss for lung nodule analysis. *IEEE transactions on medical imaging*, 39(3), 718-728.
- [16] Liu, S., & Yao, W. (2022). Prediction of lung cancer using gene expression and deep learning with KL divergence gene selection. *BMC bioinformatics*, 23(1), 1-11.
- [17] Sori, W. J., Feng, J., Godana, A. W., Liu, S., &Gelmecha, D. J. (2021). DFD-Net: lung cancer detection from denoised CT scan image using deep learning. *Frontiers of Computer Science*, 15(2), 1-13.
- [18] Suresh, S., & Mohan, S. (2020). ROI-based feature learning for efficient true positive prediction using convolutional neural network for lung cancer diagnosis. *Neural Computing and Applications*, 32(20), 15989-16009.
- [19] Yamunadevi, M. M., &Ranjani, S. S. (2021). Efficient segmentation of the lung carcinoma by adaptive fuzzy–GLCM (AF-GLCM) with deep learning based classification. *Journal of Ambient Intelligence and Humanized Computing*, 12(5), 4715-4725.
- [20] Sori, W. J., Feng, J., & Liu, S. (2019). Multi-path convolutional neural network for lung cancer detection. *Multidimensional Systems and Signal Processing*, 30(4), 1749-1768.
- [21] Iandola, F., Moskewicz, M., Karayev, S., Girshick, R., Darrell, T., &Keutzer, K. (2014). Densenet: Implementing efficient convnet descriptor pyramids. *arXiv preprint arXiv:1404.1869*.
- [22] Hua, Y., Guo, J., & Zhao, H. (2015, January). Deep belief networks and deep learning. In *Proceedings of 2015 International Conference on Intelligent Computing and Internet of Things* (pp. 1-4).
- [23] Elleuch, M., &Kherallah, M. (2019, December). Convolutional Deep Learning Network for Handwritten Arabic Script Recognition. In *International Conference on Hybrid Intelligent Systems* (pp. 103-112). Springer, Cham.
- [24] Dorigo, M., &Stützle, T. (2019). Ant colony optimization: overview and recent advances. *Handbook of metaheuristics*, 311-351.
- [25] Wibisono, A., Adibah, J., Priatmadji, F. S., Viderisa, N. Z., Husna, A., &Mursanto, P. (2019, November). Performance Analysis of Deep Learning Network Models of Localized Images in Chest X-ray Decision Support System. *International Conference on Big Data Research* (pp. 54-59).
- [26] Bhandary, A., Prabhu, G. A., Rajinikanth, V., Thanaraj, K. P., Satapathy, S. C., Robbins, D. E., ... & Raja, N. S. M. (2020). Deep-learning framework to detect lung abnormality–A study with chest X-Ray and lung CT scan images. *Pattern Recognition Letters*, 129, 271-278.
- [27] Bharati, S., Podder, P., &Mondal, M. R. H. (2020). Hybrid deep learning for detecting lung diseases from X-ray images. *Informatics in Medicine Unlocked*, 20, 100391.
- [28] E. Aarthi, S. Jana, W. Gracy Theresa, M. Krishnamurthy, A. S. Prakaash, C. Senthilkumar, S. Gopalakrishnan (2022), Detection and Classification of MRI Brain Tumors using S3-DRLSTM Based Deep Learning Model. *IJEER* 10(3), 597-603. DOI: 10.37391/IJEER.100331.
- [29] Chitra, T., Sundar, C., & GOPALAKRISHNAN, S. (2022). Investigation and Classification of Chronic Wound Tissue images Using Random Forest Algorithm (RF). *International Journal of Nonlinear Analysis and Applications*, 13(1), 643-651. doi: 10.22075/ijnaa.2021.24438.2744
- [30] Vaqur, M. ., Kumar, R. ., Singh, R. ., Umang, U., Gehlot, A. ., Vaseem Akram, S. ., & Joshi, K. . (2023). Role of Digitalization in Election Voting Through Industry 4.0 Enabling Technologies. *International Journal on Recent and Innovation Trends in Computing and Communication*, 11(2), 123–130. <https://doi.org/10.17762/ijritcc.v11i2.6136>
- [31] Jóhann, Þorvaldsson, Koskinen, P., Meer, P. van der, Steiner, M., & Keller, T. Improving Graduation Rates in Engineering Programs Using Machine Learning. *Kuwait Journal of Machine Learning*, 1(1). Retrieved from <http://kuwaitjournals.com/index.php/kjml/article/view/110>